J. Fluid Mech. (2026), *vol.* 1031, A32, doi:10.1017/jfm.2025.11049

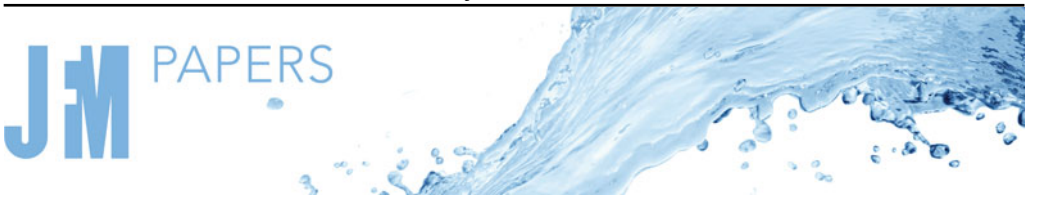

Mechanism transition of superlinear scaling in hydrodynamic dispersion

Yang Liu[1], **Yuedi Wang**[1] **and Moran Wang**[1]

[1]Department of Engineering Mechanics and SKL of ASP, Tsinghua University, Beijing 100084, PR China
Corresponding author: Moran Wang, moralwang@jhu.edu; mrwang@tsinghua.edu.cn

(Received 8 February 2025; revised 17 October 2025; accepted 10 December 2025)

The superlinear scaling relationship between the hydrodynamic dispersion coefficient and the Péclet number in porous media has been widely acknowledged. Nevertheless, the mechanisms driving this behaviour remain inadequately understood. In this work, we investigate the mechanism responsible for this superlinear scaling using a Lagrangian framework that combines a statistical model, which links the global probability density function of tracer transition time to flow variability in porous media, with a continuous time random walk framework. Our analysis reveals that the intra-pore and inter-pore flow variabilities are the primary sources responsible for the superlinear scaling, with their relative significance characterised by a structure-specific parameter, χ. Specifically, the inter-pore flow variability dominates when $\chi > 1$, while the intra-pore variability prevails for $0 < \chi < 1$. The parameter χ is derived exclusively from the statistical distributions of pore-throat radius, length and orientation angle, which can be readily obtained from structural characterisation techniques such as X-ray computed tomography imaging. These theoretical predictions are validated through extensive numerical simulations on tube networks with substantial structural variation. This study resolves discrepancies in previous studies regarding the mechanisms of superlinear scaling in hydrodynamic dispersion and offers valuable insights into modulate dispersion and mixing in porous media.

Key words: porous media, dispersion

1. Introduction

The transport of solutes through porous media is a fundamental topic with broad applications, including microcirculation in the human brain (Goirand, Le Borgne & Sylvie 2021), carbon dioxide sequestration in geological formations (Bolster 2014; Huppert & Neufeld 2014), and the delivery of gas and electrolytes in fuel cells (Peng *et al.* 2020). This process is primarily driven by the physical mechanisms of advection and diffusion, which are typically described using the advection–diffusion equation. However,

applying this equation requires a precise resolution of the pore structure, which can be prohibitively complex and resource intensive, especially for intricate media like brain tissue or sedimentary rocks, making the approach challenging and often impractical.

As an alternative, dispersion theory provides an upscaled description of the transport without requiring precise structural resolution. By averaging velocity variations below a defined scale, hydrodynamic dispersion effectively models solute transport within a reference frame moving at the mean velocity. However, flow variations in porous media occur at both the intra-pore and inter-pore levels. Intra-pore flow variability arises from no-slip boundary conditions (Saffman 1959) and irregular pore wall surfaces (Sahimi & Imdakm 1991), leading to non-uniform velocity distributions within individual pores. Conversely, inter-pore flow variability stems from the disordered pore network (Bruderer & Bernabé 2001; Sahimi & Imdakm 1988), which creates preferential flow paths and stagnant zones (Liu *et al.* 2024*a*). Together, these intra-pore and inter-pore variations intensify the overall flow variability, significantly affecting dispersion within the porous medium.

The dispersion coefficient plays a fundamental role in dispersion theory, encapsulating the effects of unresolved flow variations on solute transport and quantifying the ability of the medium to disperse solutes. Extensive experimental data demonstrate that hydrodynamic dispersion in disordered media, such as bead packs and sand packs, exhibits distinct scaling regimes between the dispersion coefficient and the Péclet number (Delgado 2005; Sahimi 2011; Bear 2013). The Péclet number measures the ratio of advection to diffusion, where higher values signify a stronger dominance of advection. In the Péclet number range of $10^0 < Pe < 10^3$, often called the 'power-law regime', the dispersion coefficient follows a superlinear scaling with the Péclet number, represented by $D_L/D_m \sim Pe^{\kappa}$, where D_L is the longitudinal dispersion coefficient, D_m represents the molecular diffusion coefficient, and the value of κ is around 1.2. At higher Péclet numbers, within $10^3 < Pe < 10^6$, known as the 'convective regime', this relationship shifts to a linear scaling, expressed as $D_L/D_m \sim Pe$.

The mechanisms underlying the superlinear scaling behaviour remain poorly understood. Conflicting perspectives exist regarding the influence of intra-pore flow variability. Some studies suggest that intra-pore flow variability is essential for producing this behaviour (Saffman 1959; Torelli 1972; Koch & Brady 1985; Sahimi *et al.* 1986; Jha, Bryant & Lake 2011; Mehmani & Balhoff 2015). In contrast, other studies demonstrate that, even without considering intra-pore flow variability, a certain degree of structural disorder within the pore network alone can yield superlinear scaling between the dispersion coefficient and the Péclet number (De Arcangelis *et al.* 1986; Bijeljic & Blunt 2006; Acharya *et al.* 2007; Van Milligen & Bons. 2014). These conflicting viewpoints are largely attributed to variations in the pore structures used across studies. Specifically, these variations manifest in pore size distribution (De Arcangelis *et al.* 1986; Bijeljic & Blunt 2006; Acharya *et al.* 2007; Van Milligen & Bons. 2014), coordination number (Sahimi *et al.* 1986; Jha *et al.* 2011; Mehmani & Balhoff 2015) and domain size (Bijeljic & Blunt 2006; Jha *et al.* 2011; Mehmani & Balhoff 2015). These structural variations can significantly influence the scaling relationship between the dispersion coefficient and the Péclet number (Bruderer & Bernabé 2001). Puyguiraud, Gouze & Dentz (2021) investigate hydrodynamic dispersion in porous media with varying structures using a continuous time random walk (CTRW) model. Their research revealed that superlinear scaling behaviours are influenced by the global probability distribution function (PDF) of tracer transition times, which may follow either a $Pe^{2-\theta}$ or $Pe\ln(Pe)$ scaling relationship. However, their study does not fully address how structural factors influence flow variability and, ultimately, shape the global PDF of transition times. Since flow variability plays a crucial

role in the evolution of Lagrangian velocity fields and, consequently, in the solute transport dynamics (Dentz *et al.* 2016; Aquino & Le Borgne 2021), this limitation hinders a deeper understanding of the mechanisms driving different superlinear scaling behaviours. To bridge this gap, Liu *et al.* (2024*c*) developed a stochastic model that explicitly accounts for the effects of both intra-pore and inter-pore flow variability on hydrodynamic dispersion. Their analysis revealed that dispersion exhibits distinct scaling regimes depending on the dominant source of flow variability. Specifically, when inter-pore flow variability dominates, dispersion follows a superlinear scaling of $Pe^{2-\theta}$ at moderate Péclet numbers, transitioning to a linear scaling at higher Péclet numbers. In contrast, when intra-pore flow variability dominates, the scaling takes the form of $Pe\ \ln(Pe)$. However, the study by Liu *et al.* (2024*c*) presents two main limitations. First, their classification of the dominant regime governing superlinear scaling relies on the properties of the PDF, $\hat{\psi}_\zeta(t)$, characterised by the parameters θ and ζ_{max}/ζ_{min}, where ζ represents the advection time of a particle through a tube, while θ denotes the power exponent of the PDF of ζ. These parameters are *a posteriori* quantities that cannot be directly derived from experimentally measurable properties. Second, the model assumes that structural heterogeneity arises solely from variations in pore size, overlooking other critical microstructural features – such as coordination number and conduit orientation – that can substantially influence flow statistics. These limitations underscore the necessity of a physically meaningful and experimentally accessible parameter to classify superlinear scaling regimes, as well as for further validation of the model across porous media exhibiting diverse forms of structural heterogeneity.

This study addresses these limitations by investigating the superlinear scaling behaviours in hydrodynamic dispersion in porous media with varying structural disorders. This work builds upon the theoretical framework developed by Liu *et al.* (2024*c*), which integrates a stochastic model that links the global PDF of tracer transition times to flow variability in porous media with a CTRW model. We begin by identifying the specific conditions under which hydrodynamic dispersion is predominantly governed by either intra-pore or inter-pore flow variability. These conditions are encapsulated by an integrated parameter, referred to as χ, which distinguishes whether the superlinear scaling behaviour is driven by intra-pore or inter-pore flow variability across different porous media. To validate the theoretical predictions, we employ network models to simulate fluid flow and solute transport through diverse tube networks exhibiting a wide range of χ values.

This paper is structured as follows. Section 2 introduces a Lagrangian framework that models solute transport in porous media by representing it as tracer transitions through a network of interconnected tubes. Within this framework, an integrated parameter, χ, is proposed to evaluate the relative impacts of intra-pore and inter-pore flow variability on superlinear scaling behaviour. Section 3 details the network model employed to simulate flow and dispersion in porous media. Section 4 validates the theoretical predictions through comprehensive numerical simulations. Finally, § 5 concludes the paper by summarising the main findings and outlining limitations of this study.

2. Transition analysis based on flow network

This study investigates hydrodynamic dispersion in statistically homogeneous porous media. The complex pore structure is simplified as a network of pores (nodes) connected by throats (tubes), a widely adopted approach in studies of flow and transport in porous media (Fatt 1956; Sahimi & Imdakm 1988; Bijeljic, Muggeridge & Blunt 2004; Mehmani & Balhoff 2015; Liu *et al.* 2022; Zhao *et al.* 2022). In this model, pores are considered to have negligible volume, with solute fully mixed within each pore, and throats are simplified as straight tubes through which fluid flow follows the Poiseuille law.

The transport of solutes through the network is modelled within a CTRW framework (Dentz *et al.* 2004; Berkowitz *et al.* 2006), where solute transport is driven by the PDFs of transition length ℓ and transition time τ. We assume that ℓ and τ are independent random variables, with their respective PDFs denoted by $\omega(x)$ and $\psi(t)$. This assumption is supported by the observed weak correlation in tracer velocities across different pores (Bijeljic, Mostaghimi & Blunt 2011; de Anna *et al.* 2013; Dentz *et al.* 2016; Alim *et al.* 2017). Within the framework, the longitudinal dispersion coefficient is derived as

$$D_L = \frac{\langle \ell \rangle^2}{2\langle \tau \rangle} \left(\frac{\langle \tau^2 \rangle - \langle \tau \rangle^2}{\langle \tau \rangle^2} + \frac{\langle \ell^2 \rangle - \langle \ell \rangle^2}{\langle \ell \rangle^2} \right). \tag{2.1}$$

A detailed derivation of this expression is provided in the supplementary material is available at https: https://doi.org/10.1017/jfm.2025.11049, see also Dentz *et al.* (2004). Here, the moments are defined as

$$\langle \tau \rangle = \int t\, \psi(t)\, \mathrm{d}t, \quad \langle \tau^2 \rangle = \int t^2\, \psi(t)\, \mathrm{d}t, \tag{2.2}$$

$$\langle \ell \rangle = \int x\, \omega(x)\, \mathrm{d}x, \quad \langle \ell^2 \rangle = \int x^2\, \omega(x)\, \mathrm{d}x. \tag{2.3}$$

Since the PDF $\psi(t)$ generally exhibits a much broader distribution than the PDF $\omega(x)$ in porous media, this implies that $\langle \tau^2 \rangle - \langle \tau \rangle^2 / \langle \tau \rangle^2 \gg \langle \ell^2 \rangle - \langle \ell \rangle^2 / \langle \ell \rangle^2$, the longitudinal dispersion coefficient scales approximately as

$$D_L \sim \frac{\langle \ell \rangle^2}{\langle \tau \rangle} \frac{\langle \tau^2 \rangle - \langle \tau \rangle^2}{\langle \tau \rangle^2}. \tag{2.4}$$

It should be noted that (2.1)–(2.4) are valid only when the second-order moments, $\langle \tau^2 \rangle$ and $\langle \ell^2 \rangle$, exist and remain finite. This condition is always satisfied in the cases considered here. Specifically, for statistically homogeneous porous media, the finite tube lengths ensure that $\langle \ell^2 \rangle$ remains finite, while molecular diffusion imposes an upper bound on the transition time, guaranteeing that $\langle \tau^2 \rangle$ is also finite.

Equation (2.4) indicates the essential role of the global PDF of transition times, $\psi(t)$, in the scaling relationship between the dispersion coefficient, D_L, and the Péclet number, Pe. The PDF $\psi(t)$ is shaped by both intra-pore and inter-pore flow variabilities (Liu *et al.* 2024*c*), which are characterised by $\psi_t(t|\zeta)$, the local PDF of tracer transition time through an individual conduit, and $\hat{\psi}_\zeta(t)$, the PDF of minimal advection times ζ associated with the tubes that tracers choose to enter at pore junctions, respectively. The minimal advection time ζ is defined as $\zeta = l/v$, where v represents the maximal velocity within the tube.

The local PDF $\psi_t(t|\zeta)$ depends on the minimal advection time ζ through the tube and can be categorised into three distinct modes. Mode I corresponds to $\zeta < \zeta_{\mathrm{D,R}}$, where radial and axial diffusion are negligible. Tracers move along streamlines with their transition times through the tube determined by advection. Mode II arises when $\zeta_{\mathrm{D,R}} \leqslant \zeta < \zeta_{D,l}$. The tracers are fully mixed across the transverse direction, and the transition time distribution is strongly peaked near the mean advection time 2ζ. Mode III occurs when $\zeta \geqslant \zeta_{D,l}$, indicating that advection is slower than molecular diffusion; under this condition, the transition times converge to approximately $\zeta_{D,l}$. Although backward tracer motion can occur near tube entrances (Aquino & Dentz 2018), its influence on hydrodynamic dispersion is minimal and is therefore neglected in this study. Liu *et al.* (2024*c*) derive the

local PDF $\psi_t(t|\zeta)$ as

$$\psi_t(t|\zeta) = \begin{cases} 2\zeta^2 t^{-3} H(t-\zeta)H(\zeta_B - t), & (\zeta < \zeta_{D,R}), \\ \delta(t-2\zeta), & (\zeta_{D,R} \leqslant \zeta < \zeta_{D,l}), \\ \delta(t-\zeta_{D,l}), & (\zeta \geqslant \zeta_{D,l}), \end{cases} \tag{2.5}$$

where H is the Heaviside step function, and $\zeta_{D,R}$ and $\zeta_{D,l}$ represent the radial and axial diffusion times, respectively. The diffusion times are calculated as $\zeta_{D,R} = R^2/D_m$ and $\zeta_{D,l} = l^2/D_m$, where R and l represent the radius and the length of the tube, and D_m denotes the molecular diffusion coefficient. Additionally, ζ_B denotes the truncation time and is given by

$$\zeta_B = \zeta \sqrt{\frac{vR^2}{8D_m l}}. \tag{2.6}$$

The PDF $\hat{\psi}_\zeta(t)$ is determined as the flux-weighted PDF of advection times

$$\hat{\psi}_\zeta(t) = \frac{1}{\sum_{i=1}^{N_0} q_i} \sum_{i=1}^{N_0} q_i \delta(t-\zeta_i), \tag{2.7}$$

where N_0 represents the total number of tubes, q denotes the flow rate through a tube and the subscript i indexes each tube.

The PDF $\hat{\psi}_\zeta(t)$ is governed by the inter-pore flow variability, which originates from the random distribution of tube properties within the network, as illustrated in figure 1. These properties include the tube radius R, length l and orientation angle β. According to the Poiseuille law, the hydraulic conductance g of a pore throat – defined as the volumetric flow rate per unit pressure drop – scales as $g \sim R^4 l^{-1}$. Under the assumption of a uniform macroscopic pressure gradient $G = |\nabla p|$ along the mean flow direction, which is reasonable for statistically homogeneous porous media (Scheidegger 1954), the pressure drop across an individual pore throat is given by $\Delta p = Gl\cos\beta$. Consequently, the following scaling relationships are obtained:

$$q \sim R^4 G \cos\beta, \tag{2.8}$$

$$v \sim R^2 G \cos\beta, \tag{2.9}$$

$$\zeta \sim l R^{-2} G^{-1} \cos^{-1}\beta. \tag{2.10}$$

By substituting (2.8) and (2.10) into (2.7), the PDF $\hat{\psi}_\zeta(t)$ can be expressed as a function of the randomly distributed geometric properties of tubes within the network

$$\hat{\psi}_\zeta(t) = \frac{1}{\sum_{i=1}^{N_0} R_i^4 \cos\beta_i} \sum_{i=1}^{N_0} R_i^4 \cos\beta_i \delta\left(t - \Theta l_i R_i^{-2} G^{-1} \cos^{-1}\beta_i\right), \tag{2.11}$$

where $\Theta = \zeta/(lR^{-2}G^{-1}\cos^{-1}\beta)$ is a coefficient associated with the tube cross-sectional shape. Assuming all tubes possess circular cross-sections, this coefficient simplifies to $\Theta = 4\mu$, with μ denoting the fluid viscosity. Consequently, the PDF $\hat{\psi}_\zeta(t)$ is completely determined from the statistical distributions of the tube radius R, length l and orientation angle β, which can be obtained through structural characterisation such as computed tomography (CT) imaging.

The minimum and maximum advection times within the network are represented by ζ_{min} and ζ_{max}, respectively. When the ratio ζ_{max}/ζ_{min} is large, the PDF $\hat{\psi}_\zeta(t)$ can be effectively

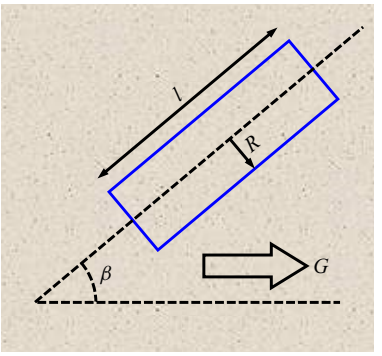

Figure 1. Schematic illustration of a single tube (blue rectangle) within the tube network. Here, R represents the tube radius, l the tube length, G the mean pressure gradient directed from left to right and β the angle between the tube axis and the mean flow direction.

modelled as a power-law function (de Anna *et al.* 2017; Dentz, Icardi & Hidalgo 2018; Liu *et al.* 2024*c*),

$$\hat{\psi}_\zeta(t) \sim t^{-2-\theta}, \quad t \in [\zeta_{min}, \zeta_{max}]. \tag{2.12}$$

Here, θ is constrained to be positive to ensure an asymptotic regime of dispersion. In contrast, when the ratio ζ_{max}/ζ_{min} is small, the PDF $\hat{\psi}_\zeta(t)$ is approximated by a Dirac-delta function (Liu *et al.* 2024*c*)

$$\hat{\psi}_\zeta(t) \sim \delta(t - \zeta_{min}). \tag{2.13}$$

The global PDF $\psi(t)$ is given by the marginalisation of the joint PDF $\psi_t(t|t')\hat{\psi}_\zeta(t')$

$$\psi(t) = \int_{\zeta_{min}}^{\zeta_{max}} \psi_t(t|t')\hat{\psi}_\zeta(t')\,\mathrm{d}t'. \tag{2.14}$$

The nature of $\psi(t)$ is shaped by the interplay between $\psi_t(t|\zeta)$ and $\hat{\psi}_\zeta(t)$, which represent intra-pore and inter-pore flow variability, respectively. Specifically, when $\hat{\psi}_\zeta(t)$ exhibits slower decay and a broader distribution than $\psi_t(t|\zeta)$, that is, when $0 < \theta < 1$ and $\zeta_{max}/\zeta_{min} > 100$ (Liu *et al.* 2024*c*), the PDF $\psi(t)$ is primarily determined by $\hat{\psi}_\zeta(t)$. In contrast, when these conditions are not satisfied, the PDF $\psi(t)$ is predominantly influenced by the PDF $\psi_t(t|\zeta)$.

Under the conditions $0 < \theta < 1$ and $\zeta_{max}/\zeta_{min} > 100$, as demonstrated in figure 2(*a*), the global PDF $\psi(t)$ follows the relation (Liu *et al.* 2024*c*)

$$\psi(t) \sim t^{-\theta-2}. \tag{2.15}$$

At intermediate Péclet numbers Pe, the transition times are constrained between ζ_{min} and $\zeta_{D,l}$. The first and second moments of the transition times scale as

$$\langle\tau\rangle \sim Pe^{-1}, \quad \langle\tau^2\rangle \sim Pe^{-\theta-1}. \tag{2.16}$$

By substituting (2.16) into (2.4), the dispersion coefficient exhibits a superlinear scaling relationship as

$$\frac{D_L}{D_m} \sim Pe^{-\theta+2}. \tag{2.17}$$

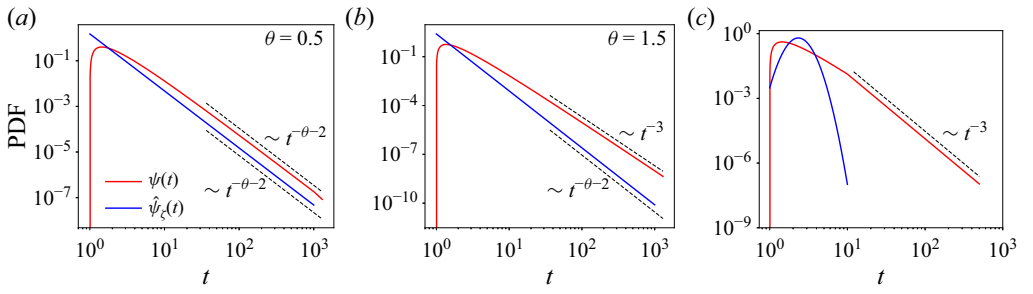

Figure 2. Comparison of the global PDF $\psi(t)$ for transition times with the flux-weighted PDF $\hat{\psi}_\zeta(t)$ for advection times in porous media with varying levels of inter-pore flow variability: (*a*) $\zeta_{max}/\zeta_{min} = 1000$ and $\theta = 0.5$, (*b*) $\zeta_{max}/\zeta_{min} = 1000$ and $\theta = 1.5$ and (*c*) small ratio of ζ_{max}/ζ_{min}. In panel (*a*), the global PDF $\psi(t)$ is primarily influenced by inter-pore flow variability, characterised by the PDF $\hat{\psi}_\zeta(t)$. In contrast, panels (*b*) and (*c*) illustrate scenarios where the global PDF $\psi(t)$ is predominantly affected by intra-pore flow variability, represented by the PDF $\psi_t(t|\zeta) \sim t^{-3}$.

In contrast, when $\theta > 1$ or $\zeta_{max}/\zeta_{min} < 100$, the global PDF $\psi(t)$ is derived as (Liu *et al.* 2024*c*)

$$\psi(t) \sim t^{-3}. \tag{2.18}$$

This behaviour is illustrated in figures 2(*b*) and 2(*c*). Under these conditions, the first and second moments of the transition times scale as

$$\langle \tau \rangle \sim Pe^{-1}, \quad \langle \tau^2 \rangle \sim Pe^{-2} \ln(Pe). \tag{2.19}$$

Consequently, the superlinear scaling relationship changes to

$$\frac{D_L}{D_m} \sim Pe \ln(Pe). \tag{2.20}$$

This logarithmic superlinear scaling is consistent with the results presented by Saffman (1959).

The variability of inter-pore flow is quantified using the coefficient of variation, defined as

$$CV = \frac{\sqrt{\langle \zeta^2 \rangle - \langle \zeta \rangle^2}}{\langle \zeta \rangle}, \tag{2.21}$$

where

$$\langle \zeta \rangle = \int_{\zeta_{min}}^{\zeta_{max}} t \hat{\psi}_\zeta(t)\, \mathrm{d}t, \quad \langle \zeta^2 \rangle = \int_{\zeta_{min}}^{\zeta_{max}} t^2 \hat{\psi}_\zeta(t)\, \mathrm{d}t. \tag{2.22}$$

A larger value of CV indicates increased variability in inter-pore flow.

For cases where $\theta \neq 1$, CV is expressed as a function of θ and the ratio ζ_{max}/ζ_{min}

$$CV = \sqrt{\frac{\theta^2}{\theta^2 - 1} \frac{\left(1 - (\zeta_{max}/\zeta_{min})^{\theta-1}\right)\left(1 - (\zeta_{max}/\zeta_{min})^{\theta+1}\right)}{\left(1 - (\zeta_{max}/\zeta_{min})^{\theta}\right)^2} - 1}. \tag{2.23}$$

For the case where $\theta = 1$, CV is expressed as

$$CV = \sqrt{\frac{1}{2} \ln\left(\zeta_{max}/\zeta_{min}\right) - 1}. \tag{2.24}$$

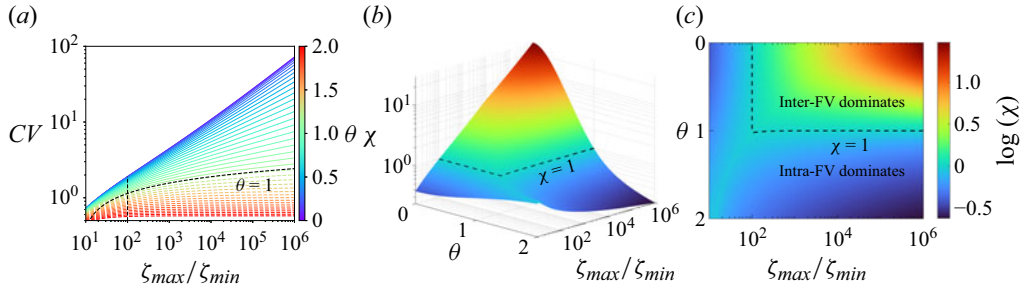

Figure 3. (*a*) Coefficient of variation for advection times (CV) in networks with varying ζ_{max}/ζ_{min} ratios and θ values. (*b*) Contour plot of χ values as a function of the ζ_{max}/ζ_{min} ratio and θ value, and (*c*) the corresponding two-dimensional projection. For $\chi > 1$, the superlinear scaling relationship is predominantly influenced by inter-pore flow variability, whereas for $\chi < 1$, intra-pore flow variability becomes the dominant factor. 'Intra-FV' and 'Inter-FV' are abbreviations for intra-pore flow variability and inter-pore flow variability, respectively.

The value of CV increases with the ratio of ζ_{max}/ζ_{min} but decreases with increasing θ, as illustrated in figure 3(*a*). This trend indicates that, when $0 < \theta < 1$ and $\zeta_{max}/\zeta_{min} > 100$, the value of CV must exceed a critical threshold CV_c, which is defined as

$$CV_c = max\{CV_{\theta=1,\zeta_{max}/\zeta_{min}}, CV_{\theta,\zeta_{max}/\zeta_{min}=100}\}. \tag{2.25}$$

As shown by the dashed lines in figure 3(*a*), the variation of CV becomes negligible when $\theta = 1$ or $\zeta_{max}/\zeta_{min} = 100$. Hence, CV_c can be reasonably approximated as

$$\begin{aligned} CV_c &\approx CV_{\theta=1,\zeta_{max}/\zeta_{min}=100} \\ &\approx 1.14. \end{aligned} \tag{2.26}$$

Although (2.23) and (2.24) define CV in terms of θ and the ratio ζ_{max}/ζ_{min}, these parameters are derived *a posteriori*. In the following, we explicitly derive CV as a function of the randomly distributed geometric characteristics of the tubes within the network. By substituting (2.11) into (2.22), the first and second moments of ζ, namely $\langle\zeta\rangle$ and $\langle\zeta^2\rangle$, are obtained as follows:

$$\langle\zeta\rangle = \frac{\Theta G^{-1}}{\sum_{i=1}^{N_0} R_i^4 \cos\beta_i} \sum_{i=1}^{N_0} R_i^2 l_i, \tag{2.27}$$

$$\langle\zeta^2\rangle = \frac{\Theta^2 G^{-2}}{\sum_{i=1}^{N_0} R_i^4 \cos\beta_i} \sum_{i=1}^{N_0} l_i^2 \cos^{-1}\beta_i. \tag{2.28}$$

Finally, substituting (2.27) and (2.28) into (2.21) yields an explicit expression for CV in terms of the geometrical properties of the network

$$CV = \sqrt{\frac{\dfrac{1}{\sum_{i=1}^{N_0} R_i^4 \cos\beta_i} \sum_{i=1}^{N_0} l_i^2 \cos^{-1}\beta_i}{\left(\dfrac{1}{\sum_{i=1}^{N_0} R_i^4 \cos\beta_i} \sum_{i=1}^{N_0} R_i^2 l_i\right)^2} - 1}. \tag{2.29}$$

Our previous work (Liu *et al.* 2024*c*) has already demonstrated that the superlinear scaling behaviour of hydrodynamic dispersion in porous media can be divided into two distinct regimes: one governed by inter-pore flow variability and the other by intra-pore flow variability. This classification, however, was based on the nature of the PDF

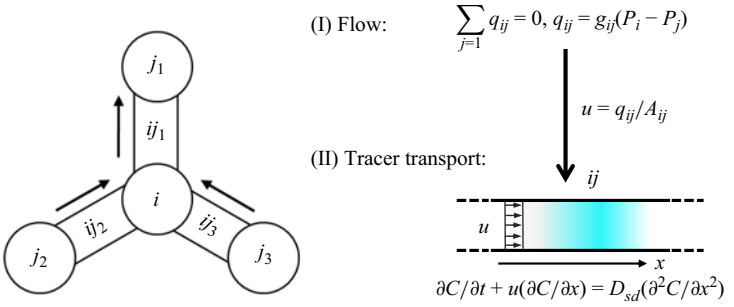

Figure 4. Schematic of flow and tracer transport between pores in the network model.

$\hat{\psi}_\zeta(t)$, characterised by the parameters θ and ζ_{max}/ζ_{min}. These parameters are *a posteriori* quantities that cannot be directly obtained from measurable properties. To overcome this limitation, the present study introduces a new dimensionless parameter, χ, defined as

$$\chi = \frac{CV}{CV_c}, \tag{2.30}$$

where CV_c and CV are given by (2.26) and (2.29), respectively. A value of $\chi > 1$ – which corresponds to $0 < \theta < 1$ and $\zeta_{max}/\zeta_{min} > 100$ – indicates that inter-pore flow variability predominantly contributes to the observed superlinear scaling behaviour. In contrast, $0 < \chi < 1$ signifies that intra-pore flow variability becomes the controlling factor, as shown in figures 3(*b*) and 3(*c*). Importantly, the value of χ is derived exclusively from the statistical distributions of the tube radius (R), length (l) and orientation angle (β) within the network, which can be obtained through structural characterisation techniques such as CT imaging.

3. Numerical methods

This section presents the network model employed to simulate fluid flow and solute transport in porous media. A comprehensive description of this model was provided in our previous work (Liu *et al.* 2022, 2024*b*); here, we present a concise overview. In this model, the pore structure is simplified as a network of pores interconnected by throats. A schematic of the numerical framework is shown in figure 4. The simulation procedure starts by determining the flow field, followed by the simulation of solute transport, both governed by mass conservation at each node.

3.1. *Network model for fluid flow*

In the network model, fluid flow through porous media is analogous to electrical current flowing through a resistor network. The flow field is determined by solving a set of linear equations constructed from local hydraulic conductance and the specified boundary conditions. The hydraulic conductance for a single tube is calculated as

$$g = \frac{\epsilon A^2}{\mu l}, \tag{3.1}$$

where A is the cross-sectional area, l is the conduit length and μ denotes the fluid viscosity. The coefficient ϵ depends on the cross-sectional shape. In this study, we consider only tubes with circular cross-sections, for which $\epsilon = 1/(8\pi)$.

The flow rate q_{ij} between two connected pores, i and j, is expressed as

$$q_{ij} = g_{ij}(P_i - P_j), \tag{3.2}$$

where P_i and P_j stand for the pressure in pore i and pore j, respectively, and g_{ij} is the hydraulic conductance of the tube connecting these two pores. Given the pressure drop between the inlet and outlet of the network, the pressure in each pore is determined by applying the mass conservation law at every pore. For example, considering pore i,

$$\sum_j q_{ij} = 0. \tag{3.3}$$

Once the pore pressures are determined, they are substituted into (3.2) to calculate the flow rate q_{ij} for each tube. Subsequently, the mean velocity within each tube is calculated as

$$u = \frac{q_{ij}}{A}. \tag{3.4}$$

3.2. *Network model for solute transport*

The transport of solute through the network is modelled using a mixed-cell network model, in which solute is assumed to be fully mixed within each pore. Solute transport occurs through both advection and diffusion, with the evolution of the concentration governed by mass conservation at each pore and throat. For the control volume of pore i, the mass conservation is described by

$$V_i \frac{\mathrm{d}C_i}{\mathrm{d}t} = \sum_{j\in in} q_{ij}\cdot C_{ij} - \sum_{j\in out} q_{ij}\cdot C_i + \sum_j \left(\frac{C_{ij} - C_i}{\dfrac{l_i}{D_{sd,i}A_i} + \dfrac{0.5l_{ij}}{D_{sd,ij}A_{ij}}} \right). \tag{3.5}$$

The term on the left-hand side of the equation represents the net mass accumulation within the control volume, while the terms on the right-hand side account for mass exchange due to advective inflow, advective outflow and diffusive mass exchange, respectively. Here, C and V refer to the concentration and the volume, respectively. The corresponding quantities for throat ij and pore i are denoted with the subscript ij and i, respectively. The term D_{sd} denotes the pore-scale shear dispersion coefficient, which reproduces the effect of parabolic velocity profiles on mass transfer within individual pores or throats. The value of D_{sd} is calculated as

$$\frac{D_{sd}}{D_m} - 1 = \frac{1}{192}\left(\frac{vR}{D_m}\right)^2 \left[1 - \exp\left(-2\alpha\frac{D_m\zeta}{R^2}\right)\right], \tag{3.6}$$

where α is a coefficient dependent on the shape of the conduit cross-sections, with values of 15, 10.8 and 4.8 for conduits with circular, square and triangular cross-sections, respectively. For the control volume of throat ij, the mass conservation is expressed as

$$V_{ij}\frac{\mathrm{d}C_{ij}}{\mathrm{d}t} = q_{ij}(C_{in} - C_{out}) + \frac{C_i - C_{ij}}{\dfrac{l_i}{D_{sd,i}A_i} + \dfrac{0.5l_{ij}}{D_{sd,ij}A_{ij}}} + \frac{C_j - C_{ij}}{\dfrac{l_j}{D_{sd,j}A_j} + \dfrac{0.5l_{ij}}{D_{sd,ij}A_{ij}}}, \tag{3.7}$$

where C_{in} and C_{out} are the inflow and outflow concentrations, respectively. An implicit scheme is employed to solve the concentration field.

The reliability and accuracy of our network algorithm have been validated through rigorous comparisons with direct numerical simulations solutions and experimental data,

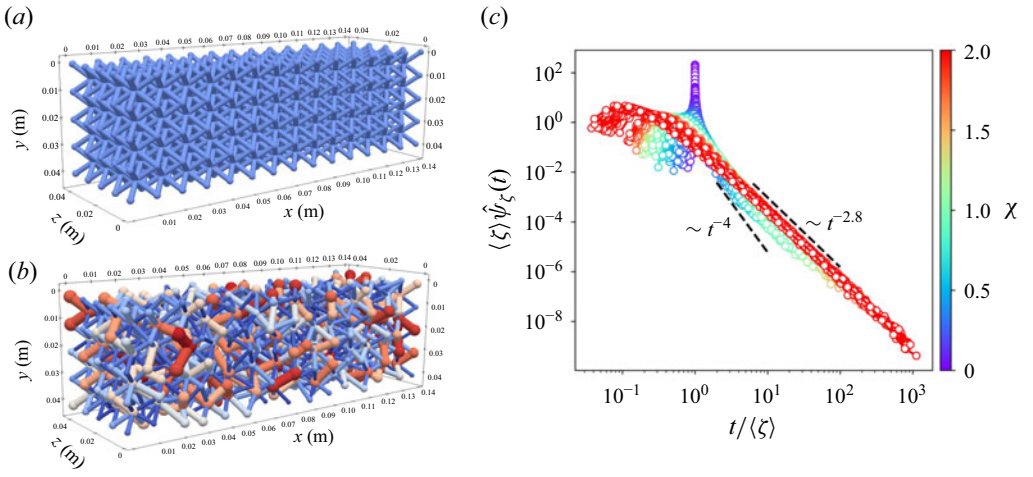

Figure 5. Illustration of the networks cropped to one eighth along the longitudinal direction: (*a*) an ordered structure, (*b*) a disordered structure and (*c*) the flux-weighted PDF $\hat{\psi}_\zeta(t)$ of advection times for the networks used in the simulations. The axis labels for the three Cartesian coordinate axes are x, y, and z, respectively, with the unit of length being meters (m).

demonstrating relative errors of less than 6 % in predicted permeability (Liu *et al.* 2022) and in predicted concentration profiles and breakthrough curves (Liu *et al.* 2024*b*).

4. Numerical results and discussion

This section presents numerical simulations of hydrodynamic dispersion in tube networks using the network model introduced in § 3. The objective is to validate the transition in the mechanisms responsible for the superlinear scaling relationship, as predicted by the analysis presented in § 2. The simulations were performed on tube networks exhibiting diverse structural characteristics, as shown in figure 5(*a*,*b*), including variations in tube diameter, coordination number, orientation and interconnectivity. These structural differences led to significant alterations in the flux-weighted PDF of advection times, $\hat{\psi}_\zeta(t)$. Specifically, the ratio of ζ_{max}/ζ_{min} and the value of θ exhibit substantial variation, as depicted in figure 5(*c*). Consequently, these variations in the PDF $\hat{\psi}_\zeta(t)$ result in substantial changes in the values of χ, which range from 0 to 2. All tube networks and the Python program for calculating χ values are provided in the Supplementary Material.

In the flow simulations, Dirichlet boundary conditions are applied to the pressure field at both the inlet and outlet, with the pressure drop adjusted to achieve the desired Péclet numbers. The global Péclet number is defined as

$$Pe = \frac{U\lambda}{D_m}, \tag{4.1}$$

where U represents the mean velocity, calculated as the total flow rate divided by the total cross-sectional area of the inlet tubes, and λ denotes the mean tube length.

For solute transport simulations, a constant concentration of C_0 is maintained at the inlet, while a zero concentration gradient is imposed at the outlet. The dispersion coefficient is determined by fitting the concentration profiles at different injection times to the analytical approximation (Gramling, Harvey & Meigs 2002)

$$\frac{C(x,t)}{C_0} = \frac{1}{2}\,\mathrm{erfc}\left(\frac{x-Ut}{2\sqrt{D_L t}}\right), \tag{4.2}$$

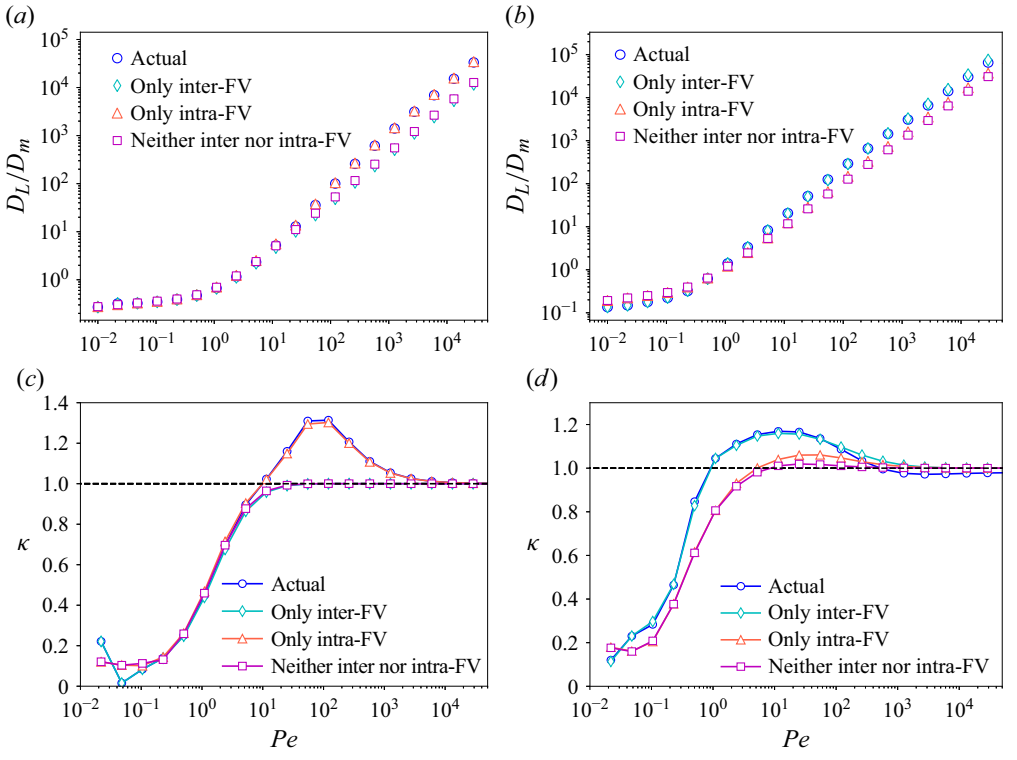

Figure 6. (*a*, *b*) Dependence of the dispersion coefficient on the Péclet number as predicted by network simulations. (*c*, *d*) Relationship between the rate of change in the logarithm of the dispersion coefficient, κ, with respect to the Péclet number. The left column illustrates results for a network with $\chi = 0.1$, whereas the right column presents data for a network with $\chi = 1.1$. A superlinear increase in the dispersion coefficient with the Péclet number is indicated when $\kappa > 1$. The label 'Actual' refers to the actual hydrodynamic dispersion, where the network model incorporates both intra-pore and inter-pore flow variability. The labels 'Only inter-FV' and 'Only intra-FV' represent scenarios where the network model incorporates exclusively inter-pore flow variability or exclusively intra-pore flow variability, respectively. The label 'Neither inter nor intra-FV' indicates cases where neither inter-pore nor intra-pore flow variability is included in the model.

where D_L is the dispersion coefficient, t is the injection time, x is the longitudinal location and C is the concentration.

The effects of intra-pore and inter-pore flow variability are examined separately. Intra-pore flow variability is disabled by excluding the effect of the parabolic velocity profile in tubes on mass transfer. This is accomplished by replacing the pore-scale shear dispersion coefficient D_{sd} in (3.5) and (3.7) with the molecular diffusion coefficient D_m. Inter-pore flow variability, on the other hand, is reflected in the heavy tail of the PDF $\hat{\psi}_\zeta(t)$, which results from stagnant zones where flow occurs at much slower rates than the average. The identification of these stagnant zones is described in detail in our previous work (Liu *et al.* 2024*a*). To deactivate the impact of inter-pore flow variability, the volumes of the pores and throats within the stagnant zones are set to zero.

Figures 6(*a*) and 6(*b*) show how the dispersion coefficient varies with the Péclet number for two distinct tube networks, characterised by χ values of (*a*) 0.1 and (*b*) 1.1, respectively. For the network with $\chi = 0.1$, the actual dispersion coefficient, which incorporates both intra-pore and inter-pore flow variability, closely matches the value obtained by considering only intra-pore flow variability. In contrast, for the network with

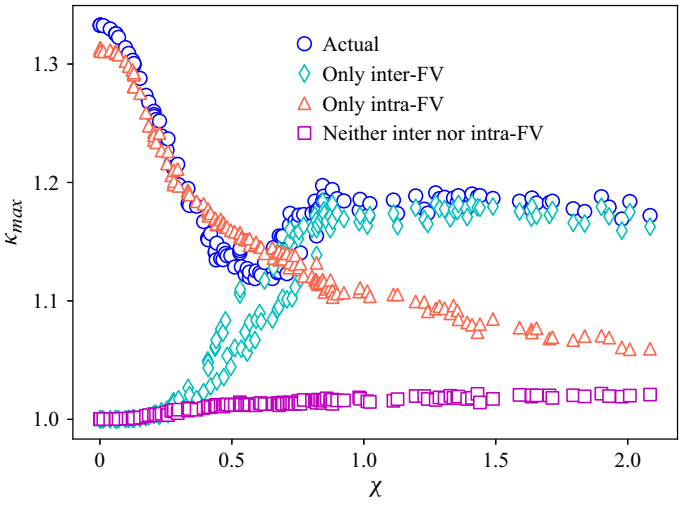

Figure 7. The relationship between κ_{max} and the parameter χ as predicted by network simulations across diverse networks. The parameter χ is calculated using (2.30). As the parameter χ increases, the primary mechanism driving superlinear scaling shifts from intra-pore flow variability to inter-pore flow variability. This transition occurs around $\chi \approx 0.7$, which closely aligns with the theoretical threshold of $\chi = 1$. The label 'Actual' refers to the actual hydrodynamic dispersion, where the network model incorporates both intra-pore and inter-pore flow variability. The labels 'Only inter-FV' and 'Only intra-FV' represent scenarios where the network model incorporates exclusively inter-pore flow variability or exclusively intra-pore flow variability, respectively. The label 'Neither inter nor intra-FV' indicates cases where neither inter-pore nor intra-pore flow variability is included in the model.

$\chi = 1.1$, the actual dispersion coefficient is nearly identical to the value obtained by considering only inter-pore flow variability.

To quantify the scaling behaviour of the dispersion coefficient with respect to the Péclet number, we define the parameter κ as the rate of change between the logarithm of the dispersion coefficient and the logarithm of the Péclet number, represented by

$$\kappa = \frac{\Delta \log(D_L/D_m)}{\Delta \log(Pe)}. \tag{4.3}$$

A superlinear increase in the dispersion coefficient to the Péclet number is indicated when $\kappa > 1$.

For actual hydrodynamic dispersion, which accounts for both intra-pore and inter-pore flow variability, the value of κ increases with the Péclet number. After reaching a peak value, κ begins to decrease and eventually stabilises at a plateau around one, indicating a superlinear scaling relationship between the dispersion coefficient and the Péclet number.

For the network with $\chi = 0.1$, the $\kappa \sim Pe$ curve for actual hydrodynamic dispersion closely matches that when only intra-pore flow variability is considered (figure 6*c*). In contrast, for the network with $\chi = 1.1$, the $\kappa \sim Pe$ curve for actual hydrodynamic dispersion aligns closely with the curve when only inter-pore flow variability is considered (figure 6*d*). These findings are consistent with the theoretical predictions presented in § 2, which suggest that for $\chi > 1$, inter-pore flow variability primarily drives the superlinear scaling behaviour, whereas for $0 < \chi < 1$, intra-pore flow variability dominates.

Due to the finite size of the tube networks employed in this study, the asymptotic scaling $D_L/D_m \sim Pe\ln(Pe)$ is not fully achieved at high Péclet numbers (see figure 6*c*). Even with networks as large as computationally feasible, hydrodynamic dispersion may remain pre-asymptotic once the Péclet number exceeds a critical threshold of $Pe_c \approx 10^3$. For

$Pe < Pe_c$, however, the results already highlight the significant impact of intra-pore flow variability on the observed superlinear scaling. Consequently, while the finite network size constrains the range over which the asymptotic regime can be observed, it does not compromise the validity of the primary conclusions.

To provide a more generalised perspective, we extract the maximum value of κ, denoted as κ_{max}, from the $\kappa \sim Pe$ curves for all the tube networks. Figure 7 illustrates how κ_{max} varies with χ. At low values of χ, κ_{max} for actual hydrodynamic dispersion closely matches that when only intra-pore flow variability is considered. This suggests that intra-pore flow variability dominates the superlinear scaling behaviour in this scenario. However, as χ increases, this trend reverses: the κ_{max} for actual hydrodynamic dispersion becomes almost identical to that when considering only inter-pore flow variability. At this stage, inter-pore flow variability dominates the superlinear scaling behaviour. The transition between these two opposing trends occurs at approximately $\chi \approx 0.7$, which is in close agreement with the theoretical threshold of $\chi = 1$. Furthermore, figure 7 indicates that, when both intra-pore and inter-pore flow variabilities are excluded, κ_{max} approaches one, signifying minimal superlinear scaling behaviour in this scenario. This indicates that both intra-pore and inter-pore flow variabilities are the primary sources driving the superlinear scaling relationship. Therefore, this study provides a comprehensive explanation of the mechanisms underlying the superlinear scaling of hydrodynamic dispersion.

The findings of this study also clarify the contradictions in previous studies regarding the mechanism of superlinear scaling in hydrodynamic dispersion. These discrepancies stem from the use of structures with varying degrees of heterogeneity, leading to significantly different values of χ. This, in turn, affects the relative contributions of intra-pore and inter-pore flow variability. For instance, both Bijeljic & Blunt (2006) and Torelli (1972) employed pore network models integrated with particle tracking to investigate hydrodynamic dispersion in tube networks with square lattice arrangements, oriented at a 45° angle to the flow direction. Despite the similarities in model set-up, their conclusions diverged: Bijeljic & Blunt (2006) concluded that inter-pore flow variability dominated the superlinear scaling law, whereas Torelli (1972) attributed the dominance to intra-pore flow variability. These conflicting results can be explained by differences in how structural disorder was incorporated into the models: Bijeljic & Blunt (2006) mapped the pore size distribution of Berea sandstone onto the network, whereas Torelli (1972) randomly removed 11 % of the network nodes. As a result, the χ values for their models differed significantly, with values of 1.2 and 0.4 for Bijeljic & Blunt (2006) and Torelli (1972), respectively. According to the transition analysis presented in § 2, these contradictory results are consistent with theoretical expectations, as the χ values for the two models are larger and smaller than 1, respectively. Furthermore, our network simulations, conducted using the same tube network, confirm the results of both studies. Detailed results of the simulations can be found in the Supplementary Material.

In this study, although both the theoretical model and PNM simulations successfully capture the transition of superlinear scaling behaviours in hydrodynamic dispersion, several limitations should be acknowledged. (i) Both the theoretical model and PNM assume zero pore volume, implying complete mixing of solute within each pore. This assumption, however, does not always hold in practice, as mixing inside individual pores is often incomplete – especially under high Péclet number conditions (Dentz *et al.* 2011). Nonetheless, Mehmani, Oostrom & Balhoff (2014) demonstrated that, for longitudinal dispersion in three-dimensional disordered porous media, the influence of incomplete intra-pore mixing on solute concentrations predicted by PNM is minor, with relative errors below 7 %. Therefore, although the zero-pore-volume assumption represents an idealisation, its impact on the present results is limited and acceptable.

(ii) The theoretical model assumes that all tubes possess circular cross-sections, whereas pore throats in real porous media typically exhibit highly irregular geometries. Variations in cross-sectional shape not only alter local velocity distributions but also contribute to inter-pore flow variability. This simplification prevents the current model from capturing these effects on superlinear scaling behaviours in hydrodynamic dispersion. Future work could parameterise the influence of cross-sectional irregularity and explicitly incorporate it into (2.8) to (2.10), thereby extending the applicability of the χ-based theoretical framework. (iii) No PNM simulations for scenarios with $0 < \theta < 0.8$ in tube networks with high ζ_{max}/ζ_{min} ratios were conducted, primarily due to the significant computational resources required to reach the asymptotic dispersion regime. Although the network model employed in this research exhibited considerable computational efficiency, the costs associated with these simulations remain prohibitive. Nevertheless, the available PNM results already provide strong evidence supporting the reliability of the χ-based model. (iv) The present study focuses exclusively on macroscopically homogeneous porous media. In heterogeneous porous structures, solute transport often exhibits anomalous behaviour (Dentz *et al.* 2004, 2020; Sahimi 2012; Kang *et al.* 2019; Puyguiraud, Gouze & Dentz 2019; Andrés *et al.* 2024; Yu *et al.* 2024; Yin *et al.* 2024), which cannot be adequately described using a conventional dispersion coefficient.

5. Conclusions

Experimental observations and numerical simulations consistently indicate a superlinear scaling relationship between the dispersion coefficient and the Péclet number in porous media. Building on our previous work (Liu *et al.* 2024*c*), which identified intra-pore and inter-pore flow variabilities as the fundamental mechanisms driving this superlinear scaling, the present study introduces a non-dimensional parameter, χ, to quantify their relative contributions. The parameter χ is derived exclusively from the statistical distributions of the tube radius (R), length (l) and orientation angle (β) within the network, which can be obtained through structural characterisation techniques such as CT imaging. The model predicts that when $\chi > 1$, the superlinear scaling is predominantly governed by inter-pore flow variability, whereas for $0 < \chi < 1$, intra-pore flow variability becomes the dominant mechanism. Extensive PNM simulations performed on networks with diverse structural heterogeneities confirm these predictions, indicating that the transition in dominance between intra-pore and inter-pore flow variability occurs near a critical threshold of $\chi \approx 0.7$, closely matching the theoretical threshold of $\chi = 1$. Furthermore, this study resolves contradictions in previous studies and provides both theoretical insights and numerical evidence regarding the mechanisms driving the superlinear scaling of hydrodynamic dispersion in porous media.

Supplementary material. Supplementary material is available at https://doi.org/10.1017/jfm.2025.11049.

Funding. This work is financially supported by the NSF of China (No.12432013, U24B6003) and the Tsinghua University Initiative Scientific Research Program.

Declaration of interests. The authors report no conflicts of interest.

Author contributions. M.W. conceived and promoted this work. Y.L. performed the simulations and theoretical derivations. Y.L. wrote the paper and M.W. revised the text. Y.W. performed the simulations and revised the text.

References

Acharya, R.C., van Dijke, M.I.J., Sorbie, K.S., Van der Zee, S.E.A.T.M. & Leijnse, A. 2007 Quantification of longitudinal dispersion by upscaling Brownian motion of tracer displacement in a 3D pore-scale network model. *Adv. Water Resour.* **30** (2), 199–213.

Alim, K., Parsa, S., Weitz, D.A. & Brenner, M.P. 2017 Local pore size correlations determine flow distributions in porous media. *Phys. Rev. Lett.* **119** (14), 144501.

Andrés, S., Dentz, M. & Cueto-Felgueroso, L. 2024 Anomalous pressure diffusion and deformation in two-and three-dimensional heterogeneous fractured media. *Water Resour. Res.* **60** (4), e2023WR036529.

de Anna, P., Le Borgne, T., Dentz, M., Tartakovsky, A.M., Bolster, D. & Davy, P. 2013 Flow intermittency, dispersion, and correlated continuous time random walks in porous media. *Phys. Rev. Lett.* **110** (18), 184502.

de Anna, P., Quaife, B., Biros, G. & Juanes, R. 2017 Prediction of the low-velocity distribution from the pore structure in simple porous media. *Phys. Rev. Fluids* **2** (12), 124103.

Aquino, T. & Dentz, M. 2018 A coupled time domain random walk approach for transport in media characterized by broadly-distributed heterogeneity length scales. *Adv. Water Resour.* **119**, 60–69.

Aquino, T. & Le Borgne, T. 2021 The diffusing-velocity random walk: a spatial-Markov formulation of heterogeneous advection and diffusion. *J. Fluid Mech.* **910**, A12.

Bear, J. 2013 *Dynamics of Fluids in Porous Media*. Courier Corporation.

Berkowitz, B., Cortis, A., Dentz, M. & Scher, H. 2006 Modeling non-fickian transport in geological formations as a continuous time random walk. *Rev. Geophys.* **44** (2), RG2003.

Bijeljic, B. & Blunt, M.J. 2006 Pore-scale modeling and continuous time random walk analysis of dispersion in porous media. *Water Resour. Res.* **42** (1), 2005WR004578.

Bijeljic, B., Mostaghimi, P. & Blunt, M.J. 2011 Signature of non-fickian solute transport in complex heterogeneous porous media. *Phys. Rev. Lett.* **107** (20), 204502.

Bijeljic, B., Muggeridge, A.H. & Blunt, M.J. 2004 Pore-scale modeling of longitudinal dispersion. *Water Resour. Res.* **40** (11), W11501.

Bolster, D. 2014 The fluid mechanics of dissolution trapping in geologic storage of CO2. *J. Fluid Mech.* **740**, 1–4.

Bruderer, C. & Bernabé., Y. 2001 Network modeling of dispersion: transition from Taylor dispersion in homogeneous networks to mechanical dispersion in very heterogeneous ones. *Water Resour. Res.* **37** (4), 897–908.

De Arcangelis, L., Koplik, J., Redner, S. & Wilkinson, D. 1986 Hydrodynamic dispersion in network models of porous media. *Phys. Rev. Lett.* **57** (8), 996–999.

Delgado, J.M.P.Q. 2005 A critical review of dispersion in packed beds. *Heat Mass Transfer* **42** (4), 279–310.

Dentz, M., Comolli, A., Hakoun, V. & Hidalgo, J.J. 2020 Transport upscaling in highly heterogeneous aquifers and the prediction of tracer dispersion at the MADE site. *Geophys. Res. Lett.* **47** (22), e2020GL088292.

Dentz, M., Cortis, A., Scher, H. & Berkowitz, B. 2004 Time behavior of solute transport in heterogeneous media: transition from anomalous to normal transport. *Adv. Water Resour.* **27** (2), 155–173.

Dentz, M., Icardi, M. & Hidalgo, J.J. 2018 Mechanisms of dispersion in a porous medium. *J. Fluid Mech.* **841**, 851–882.

Dentz, M., Kang, P.K., Comolli, A., Le Borgne, T. & Lester, D.R. 2016 Continuous time random walks for the evolution of Lagrangian velocities. *Phys. Rev. Fluids* **1** (7), 074004.

Dentz, M., Le Borgne, T., Englert, A. & Bijeljic, B. 2011 Mixing, spreading and reaction in heterogeneous media: a brief review. *J. Contam. Hydrol.* **120**, 1–17.

Fatt, I. 1956 The network model of porous media. *Trans. AIME* **207** (01), 144–181.

Goirand, F., Le Borgne, T. & Sylvie, L. 2021 Network-driven anomalous transport is a fundamental component of brain microvascular dysfunction. *Nat. Commun.* **12** (1), 7295.

Gramling, C.M., Harvey, C.F. & Meigs, L.C. 2002 Reactive transport in porous media: a comparison of model prediction with laboratory visualization. *Environ. Sci. Technol.* **36** (11), 2508–2514.

Huppert, H.E. & Neufeld, J.A. 2014 The fluid mechanics of carbon dioxide sequestration. *Annu. Rev. Fluid Mech.* **46**, 255–272.

Jha, R.K., Bryant, S.L. & Lake, L.W. 2011 Effect of diffusion on dispersion. *SPE J.* **16** (1), 65–77.

Kang, P.K., Lei, Q., Dentz, M. & Juanes, R. 2019 Stress-induced anomalous transport in natural fracture networks. *Water Resour. Res.* **55** (5), 4163–4185.

Koch, D.L. & Brady, J.F. 1985 Dispersion in fixed beds. *J. Fluid Mech.* **154**, 399–427.

Liu, Y., Gong, W., Xiao, H. & Wang, M. 2024*a* Non-monotonic effect of compaction on longitudinal dispersion coefficient of porous media. *J. Fluid Mech.* **988**, R2.

LIU, Y., GONG, W., XIAO, H. & WANG, M. 2024*b* A pore-scale numerical framework for solute transport and dispersion in porous media. *Adv. Water Resour.* **183**, 104602.
LIU, Y., GONG, W., ZHAO, Y., JIN, X. & WANG, M. 2022 A pore-throat segmentation method based on local hydraulic resistance equivalence for pore-network modeling. *Water Resour. Res.* **58** (12), e2022WR033142.
LIU, Y., XIAO, H., AQUINO, T., DENTZ, M. & WANG, M. 2024*c* Scaling laws and mechanisms of hydrodynamic dispersion in porous media. *J. Fluid Mech.* **1001**, R2.
MEHMANI, Y. & BALHOFF, M.T. 2015 Eulerian network modeling of longitudinal dispersion. *Water Resour. Res.* **51** (10), 8586–8606.
MEHMANI, Y., OOSTROM, M. & BALHOFF, M.T. 2014 A streamline splitting pore-network approach for computationally inexpensive and accurate simulation of transport in porous media. *Water Resour. Res.* **50** (3), 2488–2517.
PENG, X., KULKARNI, D., HUANG, Y., OMASTA, T.J., NG, B., ZHENG, Y., WANG, L., LAMANNA, J.M., HUSSEY, D.S. & VARCOE, J.R. 2020 Using operando techniques to understand and design high performance and stable alkaline membrane fuel cells. *Nat. Commun.* **11** (1), 3561.
PUYGUIRAUD, A., GOUZE, P. & DENTZ, M. 2019 Upscaling of anomalous pore-scale dispersion. *Transp. Porous Media* **128** (2), 837–855.
PUYGUIRAUD, A., GOUZE, P. & DENTZ, M. 2021 Pore-scale mixing and the evolution of hydrodynamic dispersion in porous media. *Phys. Rev. Lett.* **126** (16), 164501.
SAFFMAN, P.G. 1959 A theory of dispersion in a porous medium. *J. Fluid Mech.* **6** (3), 321–349.
SAHIMI, M. 2011 *Flow and Transport in Porous Media and Fractured Rock: From Classical Methods to Modern Approaches*. John Wiley & Sons.
SAHIMI, M. 2012 Dispersion in porous media, continuous-time random walks, and percolation. *Phys. Rev. E.* **85** (1), 016316.
SAHIMI, M., HUGHES, B.D., SCRIVEN, L.E. & DAVIS, H.T. 1986 Dispersion in flow through porous media – I. One-phase flow. *Chem. Engng Sci.* **41** (8), 2103–2122.
SAHIMI, M. & IMDAKM, A.O. 1988 The effect of morphological disorder on hydrodynamic dispersion in flow through porous media. *J. Phys. A Math. Gen.* **21** (19), 3833.
SAHIMI, M. & IMDAKM, A.O. 1991 Hydrodynamics of particulate motion in porous media. *Phys. Rev. Lett.* **66** (9), 1169.
SCHEIDEGGER, A.E. 1954 Statistical hydrodynamics in porous media. *J. Appl. Phys.* **25** (8), 994–1001.
TORELLI, L. 1972 Computer simulation of the dispersion phenomena occurring during flow through porous media, using a random maze model. *Pure Appl. Geophys.* **96** (1), 75–88.
VAN MILLIGEN, B.P. & BONS., P.D. 2014 Simplified numerical model for clarifying scaling behavior in the intermediate dispersion regime in homogeneous porous media. *Comput. Phys. Commun.* **185** (12), 3291–3301.
YIN, T., MAN, T., ZHANG, P. & GALINDO-TORRES, S.A. 2024 Péclet-number-dependent longitudinal dispersion in discrete fracture networks. *Water Resour. Res.* **60** (12), e2024WR038437.
YU, X., DENTZ, M., SUN, H. & ZHANG, Y. 2024 Impact of microscale physics in continuous time random walks for hydrodynamic dispersion in disordered media. *Phys. Rev. Fluids* **9** (3), 034502.
ZHAO, J., QIN, F., KANG, Q., QIN, C., DEROME, D. & CARMELIET, J. 2022 A dynamic pore network model for imbibition simulation considering corner film flow. *Water Resour. Res.* **58** (7), e2022WR032332.